Improved Representation of Ice Particle Masses Based on Observations in Natural Clouds

ANDREW J. HEYMSFIELD, CARL SCHMITT, AND AARON BANSEMER

National Center for Atmospheric Research, Boulder, Colorado

CYNTHIA H. TWOHY

Oregon State University, Corvallis, Oregon

(Manuscript received 17 March 2010, in final form 5 May 2010)

ABSTRACT

The mass–dimensional relationship put forth by Brown and Francis has been widely used for developing parameterizations for representing ice cloud microphysical properties. This relationship forms the cornerstone for past and forthcoming retrievals of ice cloud properties from ground-based and spaceborne active and passive sensors but has yet to be rigorously evaluated. This study uses data from six field campaigns to evaluate this mass–dimensional relationship in a variety of ice cloud types and temperatures and to account for the deviations observed with temperature and size, based on properties of the ice particle ensembles. Although the Brown and Francis relationship provides a good match to the observations in a mean sense, it fails to capture dependences on temperature and particle size that are a result of the complex microphysical processes operative within most ice cloud layers. Mass–dimensional relationships that provide a better fit to the observations are developed.

1. Introduction

Improved parameterizations of ice cloud microphysical properties for weather forecast models and general circulation models and accurate retrievals of ice cloud water content (IWC) and effective radius r_e from spaceborne active and passive remote sensors (e.g., onboard CloudSat, the forthcoming Earth Clouds, Aerosols, and Radiation Explorer (EarthCARE), and the *Aqua* and *Terra* satellites) are necessary to reliably simulate global climate and its change and to evaluate and improve the models. A key component of ice microphysical modules used for such studies is the assumed ice particle bulk density ρ_i or a related quantity, the ice particle mass m. The mass is usually expressed in the form $m = aD^b$, where D is taken to be a representation of particle size and a and b are empirically derived terms; $\rho_i = m/[(\pi/6)D^3]$. It is often assumed for simplicity and computational considerations that ρ_i is a constant value: a is constant and $b = 3$ (e.g., Lin et al. 1983). The next level of sophistication involves consideration of the dependence of ice particle mass on size. Although habit-dependent relationships have been developed (Mitchell 1996), the ice crystal habit is often not known and in general habits are mixed and complex. For that reason, it is desirable to have an $m(D)$ relationship that applies to a wide range of conditions. The relationship (in cgs units) $m = 0.002\,94D^{1.9}$ (Brown and Francis 1995, hereafter BF95) has been used and cited in more than 104 refereed articles in the formal literature as of December 2009. The publication topics employing this relationship include: radar/lidar/passive remote sensing (including spaceborne) retrievals (55), deriving IWC or related parameters from aircraft particle probes (28), microphysical modeling and parameterization development (15), and estimating ice cloud radiative properties and albedos (6). The coefficients used by BF95, $a = 0.002\,94$ and $b = 1.9$, are taken from work by Locatelli and Hobbs (1974, hereafter LH74), specific to aggregates of unrimed bullets, columns, and side planes. As elaborated upon later, this relationship was developed and tested from a surprisingly limited range of observations. If m were biased by a factor of $\pm 50\%$, the IWC and r_e would change by this

Corresponding author address: Andrew Heymsfield, National Center for Atmospheric Research, 3450 Mitchell Lane, Boulder, CO 80301.
E-mail: heyms1@ucar.edu

DOI: 10.1175/2010JAS3507.1

amount, the IWC retrieved from radar reflectivity by about ±15% (Hogan et al. 2006), the terminal velocity $v_t = \alpha(m)^{0.5}$ by about −30% to +40%, and precipitation rate derived from radar reflectivity by −60% to +80% [see Sekhon and Srivastava (1970), their Eq. (44)]. The goal of this article is to test, evaluate, and, if necessary, improve upon the coefficients used in the BF95 $m(D)$ relationship, with the ultimate goal of understanding how ice particles grow in natural clouds and improving ice microphysical parameterizations and retrieval algorithms, since ice microphysical properties are highly dependent on ice particle mass.

LH74, characterizing ice and snow particle masses and terminal velocities at the ground in the Cascades of Washington, developed the $m(D)$ relationship used by BF95 from a fit through data for 19 ice particles/aggregates of assemblages (polycrystals rather than single pristine crystals) of plates, side planes, bullets, and columns, characteristic of single ice particles that developed at temperatures T below −25°C and then aggregated as they fell to the collection site at the ground with temperatures above −10°C. Particle sizes (area equivalent diameter) spanned the range 1–3 mm. BF95 collected in situ data during two research aircraft flights in cirrus/ice cloud layers that extended over a vertical depth of 2–3 km. There were a total of 2650 5-s average particle size distribution (PSD) and coincident total condensate mass data (e.g., IWC), measured using a combination of evaporative total water substance measurements and Lyman-alpha fluorescence measurements of the vapor phase, peaked at about 0.1 g m^{-3} used in the analysis. Sampling temperatures were predominantly in the −20° to −30°C temperature range (P. Brown 2010, personal communication). They calculated the IWCs by summing masses derived from the LH74 study across the ice PSD as measured by a 2DC ($50 < D < 800$ μm) and 2DP probe (200–6400 μm). They found that the LH74 mass dimensional relationship for aggregates of assemblages of polycrystals provided a good fit to the directly measured IWC when integrated over the PSD. In the IWC calculation process, it was necessary to cap the $m(D)$ relationship at $\rho_i = 0.91$ g cm^{-3} and to assume spherical ice for $D <$ 97 μm where the relationship produces masses higher than for spherical solid ice particles. The crystal habits were subjectively determined from 2D probe image data to be predominantly quasi-spherical irregulars, with occasional bullet rosettes and columns, not unlike the LH74 particles. Recent studies have used an approach similar to BF95, with in situ measurements of particle size distributions and direct measurements of the ice water content for midlatitude synoptically and convectively generated ice clouds to estimate $m(D)$ relationships that fit the observations (e.g., Heymsfield et al. 2004a,b). Those studies

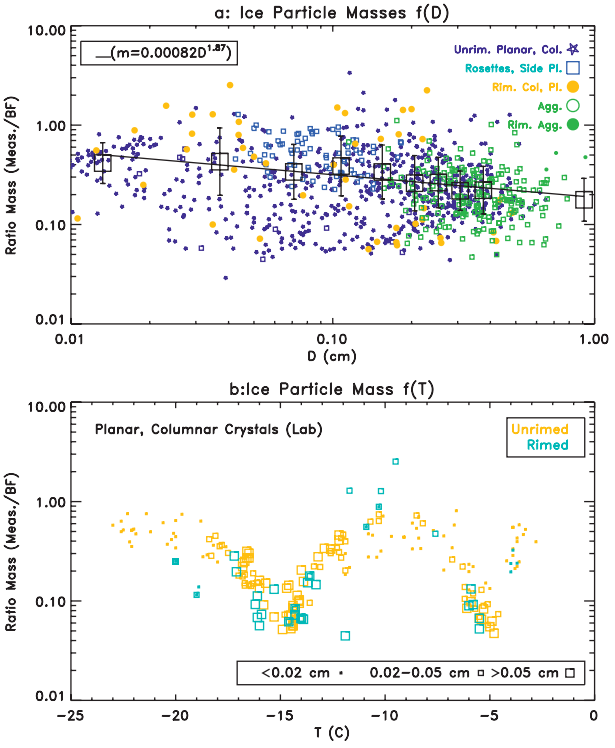

FIG. 1. Ratio of particle mass as derived from the BF95 relationship for a given particle size divided by the mass as measured. (a) Data for a number of particle types from sources given in the text. (b) Data from Takahashi and Fukuta (1988) and Takahashi et al. (1991) from laboratory experiments for unrimed and rimed ice particles grown at constant temperatures.

show values of b ranging from 2.4 (synoptic) to 2.05 (convective), although a value of $b = 1.9$ with somewhat higher values of the coefficient a would have still fit the observations but have a larger uncertainty.

In addition to the work of LH74, there have been numerous studies of ice particle masses measured both in natural and laboratory-grown environments. Examples of such data are shown relative to the mass given by the BF95 $m(D)$ relationship assuming the same D (maximum diameter) in Fig. 1. Because planar crystals that develop when $-18°C < T < -12°C$ grow linearly at rates faster than crystals of most other habits, they are amenable to both laboratory studies (Takahashi and Fukuta 1988; Takahashi et al. 1991; see our Figs. 1a,b) and field observations (Heymsfield and Kajikawa 1987; Fig. 1a). Needle crystals also grow rapidly for $-6°C < T < -4°C$ and are also amenable to laboratory studies (Figs. 1a,b). Both planar crystals and needles have masses that are relatively lower than the BF95 particles. Riming tends to increase the masses of single crystals and aggregates of a given size relative to their unrimed counterparts of the same size (Mitchell et al. 1990). During the initial stages of the growth of aggregates, they have

few component crystals and relatively low ice bulk densities (Kajikawa 1982, plotted in Fig. 1a). Side planes and bullet rosettes have masses that are comparable to those sampled in the BF95 study (Fig. 1a). Note that the largest particles in Fig. 1a are early aggregates with few component crystals and as a result very low masses when compared to well-developed aggregates.

If we *hypothetically* consider the mixture of single particles and aggregates in Fig. 1a to be a particle ensemble that might be found in an anvil, for example, we find that their masses are smaller than those predicted by the BF95 $m(D)$ relationship, with an increasingly lower fraction with increasing size and a factor of 5 difference in masses relative to BF95 at the largest sizes. If we were to simply use the $m(D)$ data without regard to cloud type or temperature, we would find an exponent b from this collective dataset of about 1.87. The LH74 and Heymsfield et al. (2004a,b) observations suggest that b may be somewhere in the range of 1.9–2.4 and with much larger implied masses.

The BF95 and other $m(D)$ relationships tested or developed for particle ensembles need to be reevaluated, for several reasons. There are three simplifications, assumptions, and qualifications in the BF95 study that differ from or qualify the LH74 $m(D)$ relationship:

- BF95 took D as the mean of the maximum chord lengths measured parallel and perpendicular to the 2DC and 2DP photodiode array (sensing) axis. This dimension is potentially very different from the maximum linear dimension of the image, especially for images that have a high axial ratio and an orientation angle somewhere between the two limits. LH74 defined D as the diameter of a sphere of equivalent cross-sectional area to the observed ice crystal. BF95 acknowledge this difference in the definition of D.
- Almost all of the BF95 IWC estimates were dominated by contributions from particles of diameters between 200 and 800 μm, whereas the LH74 particles were 1000–3000 μm.
- The BF95 observations almost all fell within the $-20°$ to $-30°$C temperature range whereas the LH74 collections were warmer than $-10°$C.

Furthermore, the BF95 and Heymsfield et al. (2004a,b) analyses should be reconsidered because 1) evidence presented since those studies indicates that shattering of ice on the inlets of the 2D-type probes can significantly enhance and thereby lead to overestimates of ice particle concentrations (e.g., Field et al. 2006, hereafter F06) at sizes that contribute significantly to the IWC and 2) new information is available to identify periods when there are significant contributions to the IWC by particles below the reliable detection thresholds of the 2D probes.

In what follows, we use data from six airborne field campaigns where PSDs and IWC are directly measured over a broad range of temperatures and cloud formation mechanisms (section 2). We evaluate the BF95 $m(D)$ relationship in the context of these observations (section 3) and draw conclusions about how ice particle masses develop as a function of their environment in natural clouds based on the analysis (section 4). Conclusions are then drawn (section 5).

2. Data

Observations presented herein include data from six field campaigns. Three of these are discussed by Heymsfield et al. (2009, hereafter H09) and in references cited therein: the Atmospheric Radiation Measurement (ARM) 2000 intensive observing period (IOP; three cold cloud cases in synoptically generated ice clouds, Oklahoma); the Cirrus Regional Study of Tropical Anvils and Cirrus Layers–Florida Area Cirrus Experiment (CRYSTAL-FACE, hereafter CF; convectively generated ice clouds, 10 cases); and the National Aeronautics and Space Administration (NASA) African Monsoon Multidisciplinary Analyses (NAMMA; 12 cases mostly convectively generated clouds, many of which formed in or near dust layers). Data we acquired during the Tropical Clouds, Convection, Chemistry, and Climate (TC4; 11 cases, Costa Rica, mostly convectively generated; see Toon et al. 2010) are also used in the analysis. Observations from synoptically generated ice cloud layers with embedded convection and liquid water from the Alliance Icing Research Study II (AIRS-2; seven cases, Toronto, Ontario, area; see Isaac et al. 2005) and the CloudSat/Cloud-Aerosol Lidar and Infrared Pathfinder Satellite Observations (CALIPSO) Validation Project (C3VP; three cases, Montreal, Quebec, area) are also examined.

Probe details are given in H09. PSDs were acquired with a 2DC or similar Droplet Measurement Technologies (DMT) Cloud Imaging Probe (CIP) probe sizing from about 50 to 1000 μm and a 2DP, DMT Precipitation Imaging Probe (PIP) or high-volume precipitation spectrometer (HVPS; 200 μm to >1 cm). Particle probe data processing methods are common across all of the above datasets, with statistically based adjustments in the concentrations measured by the imaging probes to account for shattering on their inlets (F06). A 2DS probe was also used for the TC4 analysis (Lawson et al. 2010; 20 μm to >1 mm). Liquid water was detected and its content estimated from a Rosemount icing probe (RICE), except for NAMMA. Liquid water was also detected with a King probe (ARM, CF, AIRS, C3VP). Liquid water encounters were infrequent and are identified in later discussion. Temperatures were measured with a Rosemount

temperature probe. Total condensed water content (CWC)—ice plus liquid when present—was measured with a Counterflow Virtual Impactor (CVI) or a Cloud Spectrometer and Impactor (CSI) for CWC > 0.01 g m^{-3}. The CVI (CSI) CWC is accurate to about 13% at water contents of 0.05–1.0 g m^{-3} (Heymsfield et al. 2007), but for low ice water content uncertainty increases as baseline errors become a larger percentage of actual values. Therefore, we restrict the use of the CVI (CSI) data to CWC values greater than 0.01 g m^{-3}.

3. Results

As noted earlier, the observations reported by BF95 were acquired primarily at temperatures from −20° to −30°C, with masses dominated by particles in the 200–800-μm size range and IWCs peaking at about 0.1 g m^{-3}; the sampling was conducted in stratiform cloud types produced largely by frontal lifting. Here, we consider ice cloud conditions more broadly encountered in the atmosphere: $0 < T < -60$°C, IWCs dominated by particles where $100 < D < 2000$ μm and extending to >1 g m^{-3}, and in ice clouds generated by large-scale uplift and convection. We calculate IWC from measured PSDs, averaged over 5-s intervals or about 700 m in the horizontal using the BF95 relationship and compare them to measurements from the CVI (CSI). We express the results in terms of the median mass diameter D_m—the diameter that splits the IWC distribution with D in half—and T. The D_m values were calculated in two ways: one from the measured PSDs, the other from fitted PSDs. The former are more accurate than the latter and are used here but functional forms of PSDs are relevant for modeling studies and were also examined. Gamma-type functions of the form

$$N = N_0 D^{\mu} e^{-\lambda D} \quad (1)$$

were fitted to the PSD. In Eq. (1), N_0 is the intercept, μ the dispersion, λ the slope, and D the maximum measured particle dimension as derived from a procedure that finds the minimum diameter of a circle that covers a particle. The D_m can be calculated from the fitted PSDs:

$$D_m = (b + \mu + 0.67)/\lambda \quad (2)$$

(after Mitchell 1991). Caution should be used when applying Eq. (2) to fitted PSDs that have steep slopes (dominance of small, <100-μm particles) and shallow slopes [because Eq. (2) involves an integration to infinity, far beyond the true size range]. Because the probe processing methods were similar (except for the 2DS data) for the various field programs and most of the mass is contained in sizes where the imaging probes sample reliably, differences in the results are much more likely the result of differences in the cloud particles rather than the instrumentation used.

a. Interpretation of the Brown and Francis analysis

BF95 made a number of simplifications in their analysis and were unaware of probe problems that came to light after their study was completed. We first evaluate how these factors could have affected their analysis.

1) Representation of particle diameter

BF95 took D as the mean of the maximum chord lengths measured parallel and perpendicular to the 2DC and 2DP photodiode array (sensing) axis to define a particle's diameter. Analysis of our data indicates that their D are 4% smaller, on average, than D as we define it in our study, which would lead to IWCs about 10% smaller. For simplicity, we will assume that their D is approximately the same as ours. LH74 defined D as the dimension of a circle of equivalent area to that of the particle. A reanalysis of all of the raw LH74 photographs for aggregates (Heymsfield and Westbrook 2010) indicates that the median ratio of the maximum projected dimension as we define it to the diameter used by LH74 was 1.18, which could correspond to an overestimate of particle mass relative to LH74 by 38%.

2) Shattering of large particles on the 2DC probe inlet

Unavailable to BF95 were results showing that shattering of large ice particles on the leading surfaces of 2DC probes causes enhanced concentrations of small ice (F06), artificially enhancing concentrations of ice smaller than about 200 μm. In our analysis, we have objectively removed such artifacts based on particle interarrival times and Poisson statistics (F06). Figure 2a shows the ratio of IWC calculated from the uncorrected PSDs versus IWC calculated with shattered particles removed. We have compared IWCs with and without the shattering correction as a means of estimating what impact this might have had on the BF95 analysis. The analysis suggests that this omission would have resulted in a ~10% overestimation of the IWC on the field program.

3) Small ice (<50 or 100 μm)

Cirrus PSDs can extend down to 10-μm diameter or smaller but the BF95 PSDs were not measured smaller than 50–100 μm. However, because their IWC measurements would have included such small particles, to match the measured to calculated IWC would have necessitated an overestimated value of the a coefficient. This would

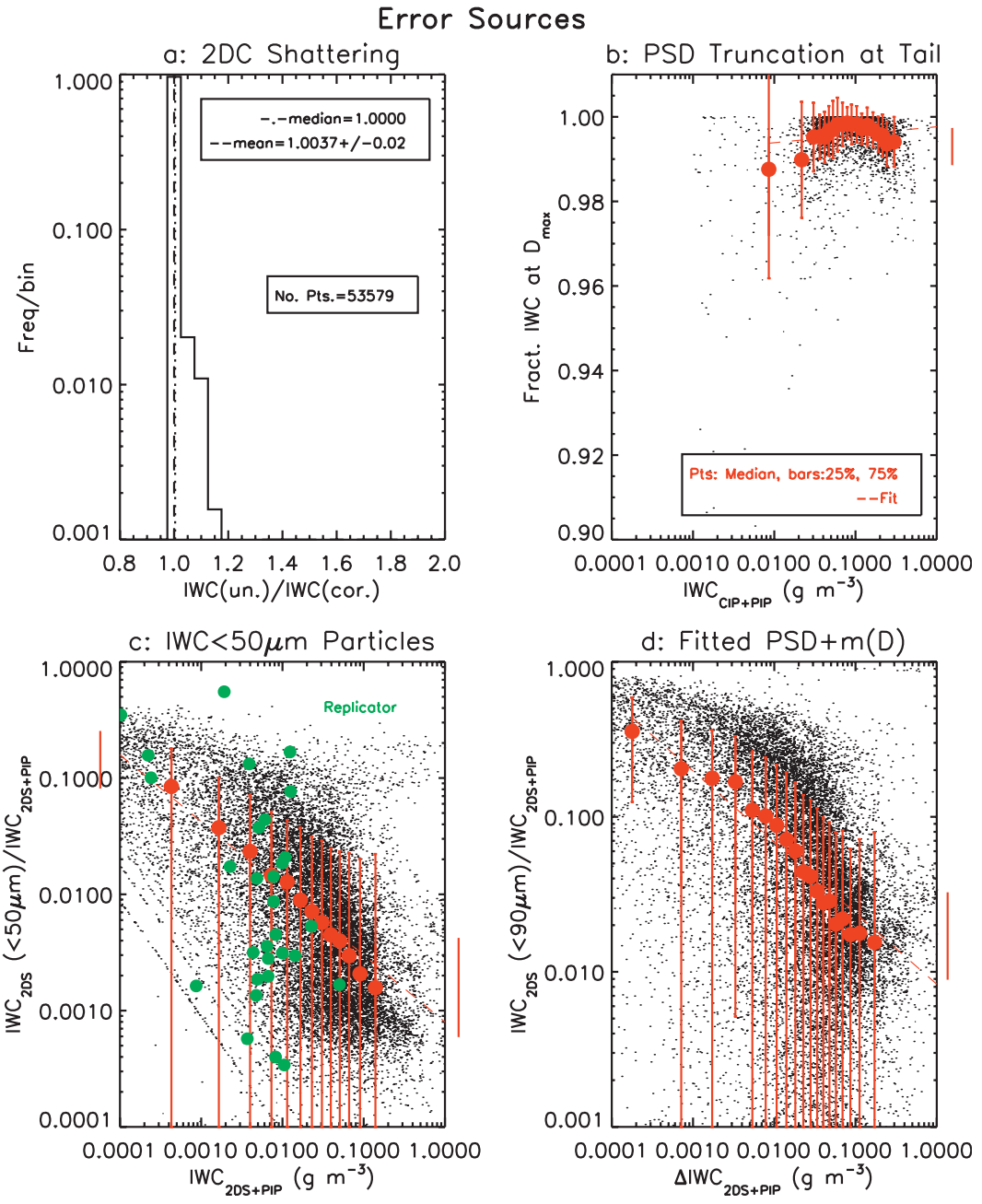

FIG. 2. Evaluation of potential error sources in the analysis of Brown and Francis and others. (a) Ratio of IWC calculated without rejection of particles suspected to be shattered on the inlets of the 2D probes (uncorrected: un.) to the IWC calculated with shattered particles removed objectively. Data from all six field programs are combined. (b) Effects of truncation at the tail of the PSD, estimated by comparing the CWC calculated by integrating PSD from 0 to the maximum size measured to that derived by integrating the fitted PSD from 0 to ∞. Data from all field programs are combined. (c) Fraction of IWC estimated in small particles as calculated from the PSD derived from the higher-resolution, lower size detection threshold 2DS probe than the 2DC for $T < 0$°C. Shown is the ratio of the IWC in >50 μm (2DS + 2DP) to the IWC measured at >10 μm as a function of the latter IWC (points, means, and error bars). Instances with supercooled liquid water as measured from the RICE probe are omitted. Colored points show the fraction of IWC estimated in <50-μm particles from balloon-borne ice crystal replicator observations in cold cirrus clouds. (d) Error resulting from analytically estimating the IWC from the BF95 without due consideration for mass overestimates for <97-μm particles.

have in part offset the differences caused by the different definition of the particle size [see section 3a(1) above].

Our analysis points to a general tendency for a decrease in the fractional contribution to the IWC by small particles with increasing IWC. This is clearly demonstrated from the 2DS data from TC4 (Fig. 2c; see also Lawson et al. 2010). The relatively small contributions of small particles to the IWC in most situations is further demonstrated using PSDs collected from the base to tops of three synoptically generated cirrus clouds ($-20°C < T < -65°C$) with our balloon-borne ice crystal replicators with a minimum detection limit of about 10–20 μm (Fig. 2c; see also Heymsfield and Iaquinta 2000).

In the appendix, we compare the IWCs derived from the 2D probe data (IWC_{2D}) to those from the small particle probes (IWC_s) from the data from four field programs. We find that there is generally a linear relationship between IWC_s and IWC_{2D}, a feature described by Heymsfield (2007) and H09 and interpreted to be the result of shattering. Those periods when IWC_s is significantly above the amount expected from shattering occur where there is a contribution by ''real'' small particles, either ice or liquid. From the analysis in the appendix, the average contribution of small (shattered + real) ice to the total IWC is about 12%–17% (for ARM, CF, and TC4; Figs. A1a,c,e), with a tendency for the ''true'' amount to decrease with IWC (Figs. A1b,d,f). Much larger amounts are noted for NAMMA as a function of CWC, which we interpret as being due to a combination of highly supercooled droplets, strong updrafts, and enhanced concentrations of small ice due to homogeneous nucleation (H09). These averages are upper limits because of the contributions to the amounts from shattered ice. In summary, contributions to the measured IWC are enhanced by small ice but primarily at low IWCs, a feature that would lead to overestimates of the a coefficient on the order of 10% for the clouds sampled here ($-60°C < T$).

4) Truncation at the PSD tail

Measured PSDs are artificially truncated at their large end because of inherent sample volume limitations, an aspect not directly considered by BF95. Given that the bulk water content probes have a much larger sample volume than the particle probes, there is again a tendency to overestimate the a coefficient to provide a match with the measured IWC.

The fitted PSDs [Eq. (2)] are used to investigate the potential loss of IWC due to the effect of truncation at the tail of the PSD spectrum. From analytic considerations,

$$\mathrm{IWC} = a\int_0^{D_{\max}} N_0 D^{\mu} D^{b} e^{-\lambda D}\, dD \quad \text{and} \qquad (3a)$$

$$\mathrm{IWC} = aN_0\Gamma(\mu + b + 1)/\lambda^{(\mu+b+1)}, \qquad (3b)$$

where Γ is the Euler gamma function. Equation (3a) can be integrated over the size range 0–$D_{\max}$, the maximum measured particle diameter, to yield an incomplete gamma function whereas Eq. (3b) assumes an integration from 0 to ∞. Using the measured size distributions, the ratio of IWCs given by Eqs. (3a) and (3b) gives us an estimate of the maximum loss in IWC due to truncation. Even though these estimates have the inherent limitation that the PSDs extend to ∞ and that they represent an upper limit, we conclude that truncation effects on the IWCs are minor (Fig. 2b).

5) Extrapolation of the $m(D)$ relationship to small sizes

Masses given by the $m(D)$ relationship exceed those for solid ice spheres, with $\rho_i = 0.91$ g cm^{-3}, when $D < 97$ μm, so a limit of $\rho_i = 0.91$ g cm^{-3} and an assumption of spherical ice particles must be placed on masses below this size. This restriction was correctly applied in BF95 but has nonnegligible effects and has not always been accounted for in studies built on the BF95 analysis. The magnitude of this error is demonstrated by comparing IWCs with and without the ρ_i limit, with the result that it is a particularly large effect at low IWC (Fig. 2d). Particular care must be taken when the $m(D)$ relationship is integrated directly with parameterized PSDs to derive IWCs.

b. *Application of the BF95 relationship to our datasets*

We now examine application of the BF95 relationship to data from the six field programs identified in section 2. Because the CVI (CSI) uncertainty is relatively large at IWCs < 0.01 g m^{-3}, which may be dominated by small particles [section 3a(3)], we cannot ascertain how well the BF95 relationship performs for IWCs smaller than 0.01 g m^{-3}. However, there is little difference in the results in a mean sense whether we use data from the 2DS with a minimum detectable size $D_{\min}$ of about 20 μm or the CIP with $D_{\min}$ of 50 μm (Figs. 3a,b). Furthermore, if we assume that the 2DS probe measures the IWC perfectly as a means of overcoming the larger CVI (CSI) uncertainty below 0.01 g m^{-3}, the ratio of the IWC from the 2DS + PIP probe to the IWC from the CIP + PIP probe is a median value of 1.04, with data extending down to temperatures of $-57°C$. If only the range $1 \times 10^{-4} < \mathrm{IWC} < 1 \times 10^{-2}$ g m^{-3} is considered, this median ratio becomes 1.17 but is likely an upper bound because the spherical ice density assumption for sizes <97 μm might yield masses a factor of 2 too large

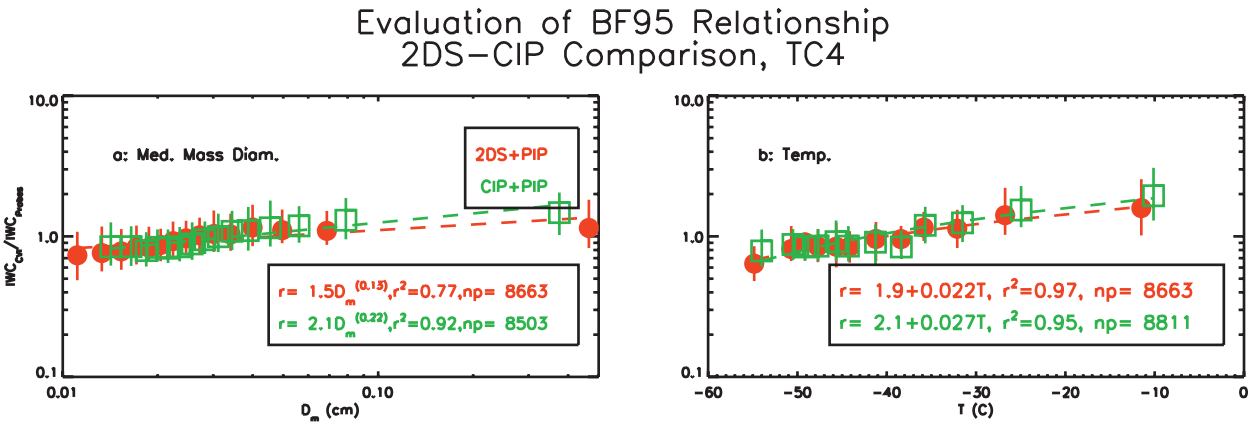

FIG. 3. Ratio of IWC measured to IWC derived from the PSDs measured by the 2DS and CIP (2DC type) probes plus the precipitation probe from TC4, as a function of (a) the D_m as derived from the measured PSDs and (b) T. Error bars extend to 25th and 75th percentiles of the points. Fits to the data are indicated and plotted.

(Schmitt and Heymsfield 2009). We therefore feel justified in drawing interpretations using CIP + PIP PSDs, especially for IWC above 0.01 g m^{-3}, although certainly there are conditions for which this oversimplification is in error (e.g., temperatures below −60°C).

Figure 3 shows that for both probe combinations the relationship between the IWC derived from the BF95 relation trend similarly and point to an underestimate in the estimated masses at small D_m and low temperatures uniformly to an overestimate at large D_m and high temperatures. The ratio of calculated to measured IWCs is not nearly as large as the factor of 5 implied by Fig. 2 but is sufficient to cause significant errors in derived properties.

We first calculate the coefficients (a, b) that provide the best match with the measured IWCs on a flight-by-flight basis to provide an overview of the analysis that follows. The particle habits can vary in the vertical for given flights and therefore this comparison is meant to provide a summary of the data that follows. Values of b from 1.5 to 2.5, bounding the range found from earlier observations, are assumed. Using each measured (5-s average) PSD, a coefficient that provides the best match with the measured IWCs on a flight-by-flight is derived. Periods when the IWCs contained in small particles are identified as being significant (see the appendix) are excluded although some such periods might not have been identifiable using the procedures discussed in the appendix. Median values of $a = f(b)$ values are found for each flight. Figure 4 shows mean values of $a = f(b)$ by research flight and averaged for all flights, respectively, separated according to primarily (top) stratiform and (bottom) convective cloud types. Standard deviations are not plotted for the individual cases to improve clarity. Increasing values of a are associated with increasing values of b. The mean, minimum, and maximum values of a are markedly lower for the stratiform than convective cases. This result implies that the values of ρ_i for the former are markedly lower than for the latter. The BF95 relationship generally overestimates a for the stratiform cases and underestimates a for the convective

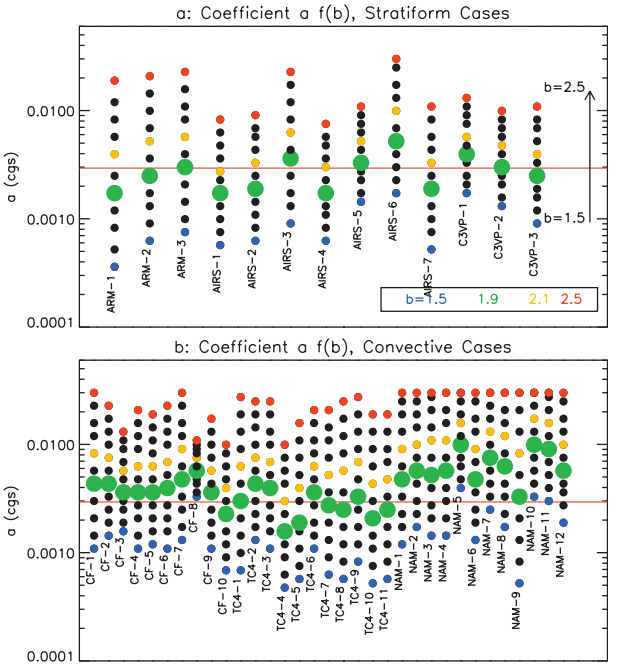

FIG. 4. For each flight day, average values of the coefficient a are derived for values of b ranging from 1.5 to 2.5 in increments of 0.1. (a) Primarily stratiform-type clouds from ARM, AIRS, and C3VP. (b) Primarily convective-type ice cloud layers from CF, TC4, and NAMMA. Horizontal lines correspond to BF95 value and large points are for $b = 1.9$.

cases. The largest underestimates are for the NAMMA cases, likely because of the prevalence of IWC in small particles associated with the vigorous updraft cores (see the appendix). Liquid water was also common in the AIRS-2 dataset and periods when it was present had to be eliminated because this would lead to an overestimate of the IWC. Note that the mean values of $a(b)$ shown in Fig. 4 are not statistical samples in that they do not consider any size or temperature dependence, a topic discussed further in section 4.

Bullet rosette–type crystals predominated in ARM-1, ARM-2, ARM-3, CF-8, and AIRS-2. Particle sizes covered extend to relatively small sizes of only several millimeters compared to other clouds sampled. The larges sizes observed for the CF-8 case were the smallest of CF cases, even though the particles developed in decaying convection. The BF95 relationship fit the observations well in these cases, presumably because this relationship works well in similar clouds and/or because the particle sizes tended to be relatively small.

We find that on average the a and b coefficients are directly related (Figs. 5a,b). The (a, b) pairs from BF95 and those from Heymsfield et al. (2004a,b) fall nearly along the fitted lines that relate a and b for the given cloud formation mechanism. The relationship found between a and b can be demonstrated analytically from Eq. (3b). Assuming a constant IWC, and assuming too that the PSDs can be integrated from 0 to ∞ with sufficient accuracy, a set of coefficients $(a1, b1)$ is related to a second set $(a2, b2)$ by

$$a2 = a1[\Gamma(b1 + \mu + 1)/\Gamma(b2 + \mu + 1)]\lambda^{b2-b1}. \quad (4)$$

For a simple exponential PSD ($\mu = 0$) and for typical values of $\lambda = 10$ and 100 cm^{-1}, increasing b from $b1 = 1.8$ to $b2 = 2.2$ produces a values of 1.1 and 1.7, respectively.

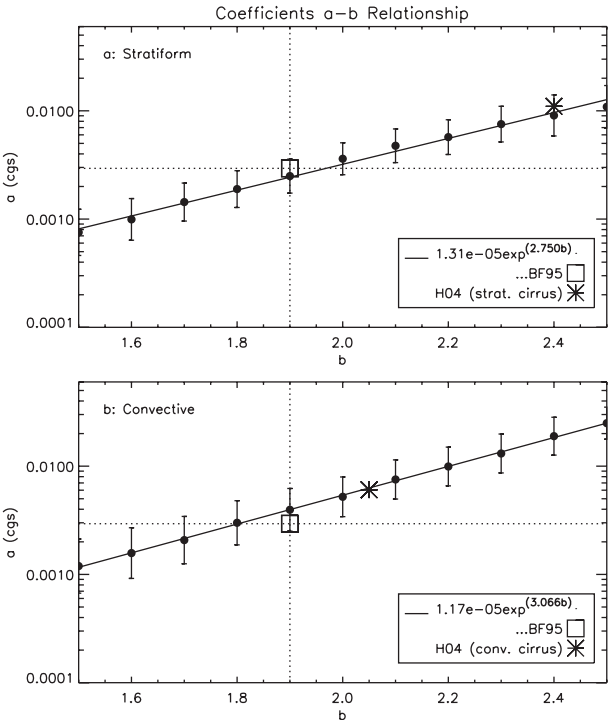

FIG. 5. Mean values of a coefficient as a function of b value for the (a) stratiform and (b) convective clouds identified in Fig. 4. Error bars show standard deviation; fit through the data points is plotted and listed.

4. Discussion

a. Improved estimate of b coefficient from CWC data and PSDs

If $b = 1.9$ applies to all ice clouds and a is biased either low or high relative to the value used by BF95, the ratio of measured to calculated IWC should be relatively independent of the mean diameter of the PSD or the temperature—that is, the error would be scaled according to the error in a. However, as with Fig. 3, a trend noted with the mean diameter (or temperature because mean ice particle sizes generally increase with temperature) would imply an error in the value of b. To a first approximation, we can take this mean diameter to be D_m. For synoptically generated ice cloud (ARM, AIRS, C3VP), the BF95 relationship overestimates the IWC at *low* D_m and low T, trending toward underestimates with increasing D_m and high T (Figs. 6a,b). This trend implies either overestimated ice densities at small sizes and underestimated densities at large sizes, or that b is larger than 1.9. Curves fitted to the ratios of measured to calculated IWCs plotted in Figs. 6a would suggest that an increase in b by about 0.2 would account for these observed trends. Scaling a with T by the amount shown in Fig. 6b would improve the match with the BF95 relationship. There are clear differences between the ARM and AIRS/C3VP datasets. Calculated IWCs are appreciably underestimated for the convectively generated ice cloud throughout the range of D_m and T for CRYSTAL-FACE and NAMMA, which were usually associated with vigorous convection (Figs. 6c,d). Vertical mixing of ice habits and PSDs through vertical motions is likely responsible for the relative independence of the ratio of measured to calculated IWCs and hence the $m(D)$ relationship with size and temperature. Convection was weaker during TC4 and the same aircraft and probes were used as in NAMMA. The lower masses are therefore attributable to the weaker convection that generated the TC4 anvils.

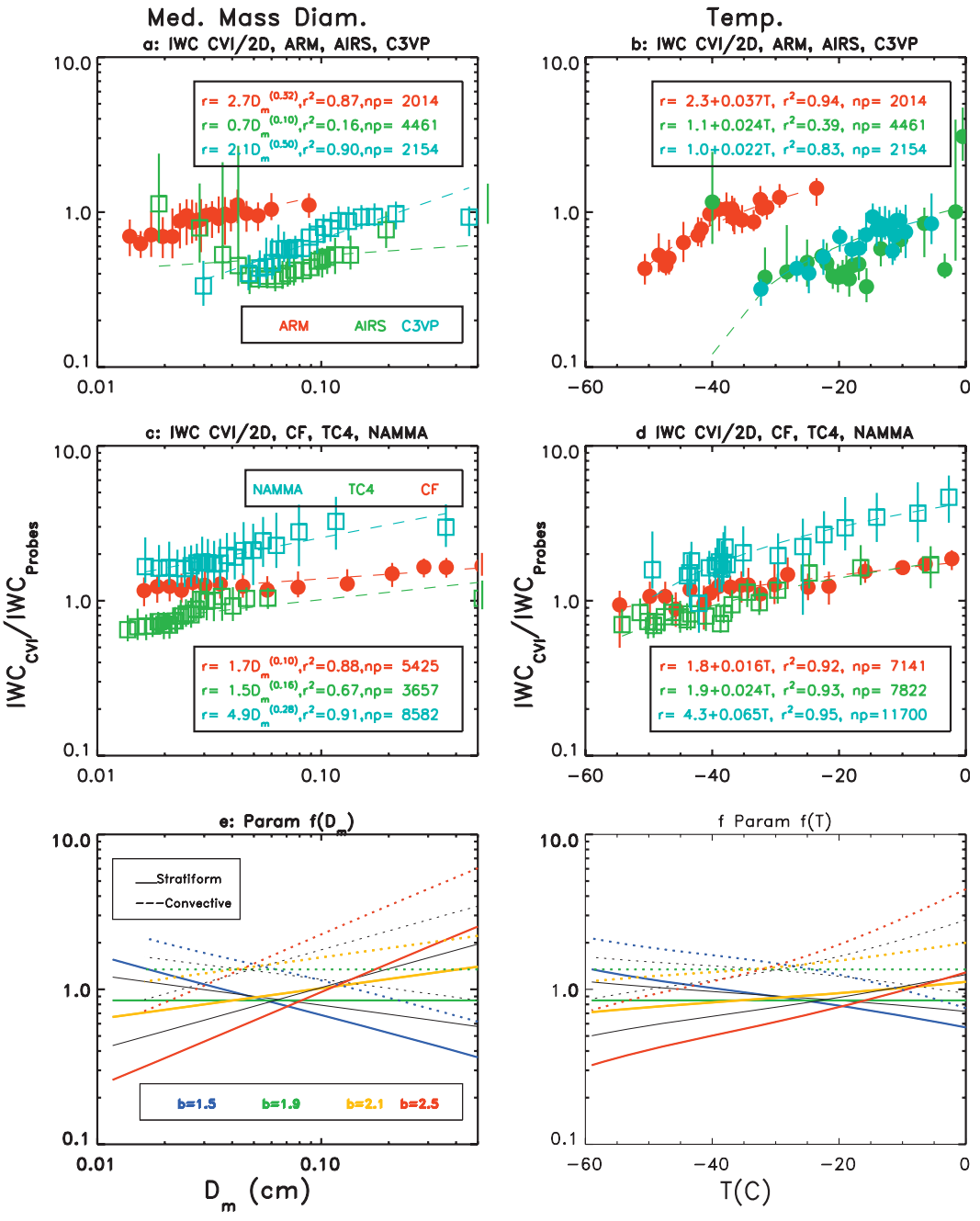

FIG. 6. (a)–(d) As in Figs. 3a,b: (left) D_m and (right) T for (a),(b) stratiform and (c),(d) convective clouds. (e),(f) Curves derived by modifying the a, b coefficients of the BF95 relationship by specifying the slope of the PSDs and using the parameterized forms of the IWC, showing dependence of the PSD dispersion and temperature on λ. Lines are in even increments of $b = 0.2$, with specific values colored.

The trends noted in the ratio r of the measured to calculated IWC as functions of D_m and T can aid in finding the values of (a, b) that better fit the observations. In Fig. 1, it is noted that an exponent of less than 1.9 in the $m(D)$ relationship produces a downward sloping relationship between the ratios of the measured to calculated (BF95) masses and D for individual particles. In Fig. 6, a value of $b = 1.9$ with a constant value of a would give values of r that have no slope with D_m and T. A varying value of a and a constant value of $b = 1.9$ could explain the trends, but for simplicity and lack of knowledge we assume that the dominant contributor to

the deviation from unity in Figs. 6a–d is due to inaccurate specification of the value of b in the $m(D)$ relationship. Future examinations comparing two bulk properties—IWC and radar reflectivity, for example—can help resolve whether variations in a and/or b values are the dominant contributors to the observed trends.

A better estimate of the value of b is derived from the trends noted in Figs. 6a–d using the analytical form of the IWC given by Eq. (3b) and D_m from Eq. (2). We assume that r_o is a value of the ordinate along one of the curves in Figs. 6a–d. If the BF95 coefficients are $a_{\rm bf}$ and $b_{\rm bf}$, then any other (a, b) pair gives

$$r = r_o\{[a_{\rm bf}\Gamma(\mu + b + 1)/\lambda^{(\mu+b_{\rm bf}+1)}] / [a\Gamma(\mu + b + 1)/\lambda^{(\mu+b+1)}]\}. \quad (5)$$

Thus, when $b = b_{\rm bf}$ and $a = a_{\rm bf}$, r reduces to r_o, but if $b = b_{\rm bf}$ and $a < a_{\rm bf}$, then r drops relative to r_o, which would correctly reduce the values of r above 1 in Figs. 6a–d, etc.

Equation (5) is applied to the datasets using relationships developed in parametric form and simplified to reduce the number of free variables in the following ways:

1) Express the variable a in terms of b. A value of b is chosen and then an appropriate value of a is derived using the functional forms $a = f(b)$ given separately for stratiform and convectively generated ice clouds in Figs. 5a,b.
2) Express μ in terms of λ. A relationship of the form

$$\mu = \sum_{i=0}^{3} c_i \lambda^i \quad (6)$$

is derived here from the PSD using a least squares fitting technique, where $c_0 = -0.6022$, $c_1 = 0.024\,417$, $c_2 = -5.1955 \times 10^{-5}$, $c_3 = 3.732\,770\,1 \times 10^{-8}$ (stratiform), and $c_0 = 1.3391$, $c_1 = 0.012\,89$, $c_2 = 7.502 \times 10^{-6}$ and $c_3 = -1.114 \times 10^{-8}$ (convective). Units are cgs.
3) PSD slopes λ are assumed to range from 1 to 500 $\rm cm^{-1}$.
4) Values for r_o are taken to be the ratio of a (where $b = 1.9$) in Figs. 5a,b to $a_{\rm bf}$.
5) To find the dependence of r on the temperature, we use our observations to develop a relationship

$$\lambda = \alpha e^{T\beta}, \quad (7)$$

where it is found that $\alpha = 14.26$ and $\beta = -0.0538$ (stratiform) and where $\alpha = 2.425$ and $\beta = -0.088$ (convective) (cgs units).
6) Temperatures are assumed to range from 0° to −60°C.

As shown in Figs. 6e,f, values of b smaller than 1.9 produce downward sloping lines with increasing D_m and T and values above 1.9 produce upward sloping lines. The values of r are higher for convective than for stratiform clouds. There is a reasonable match to the trends in $r = f(D_m)$ and $r = f(T)$ derived for $b = 2.1$ for both stratiform and convective clouds.

b. Improved estimate of the b coefficient from fractal analysis

For fractal particles, the fractal dimension is the exponent in the power-law form of the mass–dimensional relationship, that is, the coefficient b. We can therefore use fractal geometrical techniques to independently estimate b. The fractal dimension has been calculated for particles sampled by the cloud particle imager (CPI) probe that collected data during ARM, CF, and AIRS for a subset of the experimental days for each of these campaigns using the box counting method (Falconer 2003). To estimate the fractal dimension of a 2D image, a square grid is superimposed over the image. The number of grid squares that include part of the particle is counted and saved along with the grid size. The grid size is then increased, and again the grid squares that include part of the particle are counted. This process is repeated by increasing the grid size slowly until the grid squares reach 15% of the maximum size of the particle. The fractal dimension is the slope of a graph relating the number of occupied grid squares to grid size. The two-dimensional fractal dimension values for the particle images have been converted into three-dimensional fractal dimension values based on the technique described in Schmitt and Heymsfield (2010).

Figure 7 shows the trends with temperature in the median fractal dimension values for the particles in four size ranges ranging from 100 to 2000 microns as acquired during Lagrangian spiral descents through four ice cloud layers. The median and mean fractal dimensions differed insignificantly and the standard deviation was uniformly about 0.07 except for AIRS 2, which had higher standard deviations due to habit mixtures in some temperature ranges. Figures 7a and 7b show fractal dimension results from two CF flights (corresponding to CF-9 and CF-4 in Fig. 4) through anvils that were dominated by aggregates. As convective clouds are well mixed, the particle shapes and fractal dimensions did not vary much with altitude. Additionally, the fractal dimension increased with particle size. The stratiform cases (Figs. 7c,d) were dominated by pristine ice rather than aggregates. The uniform shapes observed for the ARM case (ARM-2, Fig. 4), mostly bullet rosettes, produced stable fractal dimension values with temperature, although the smallest

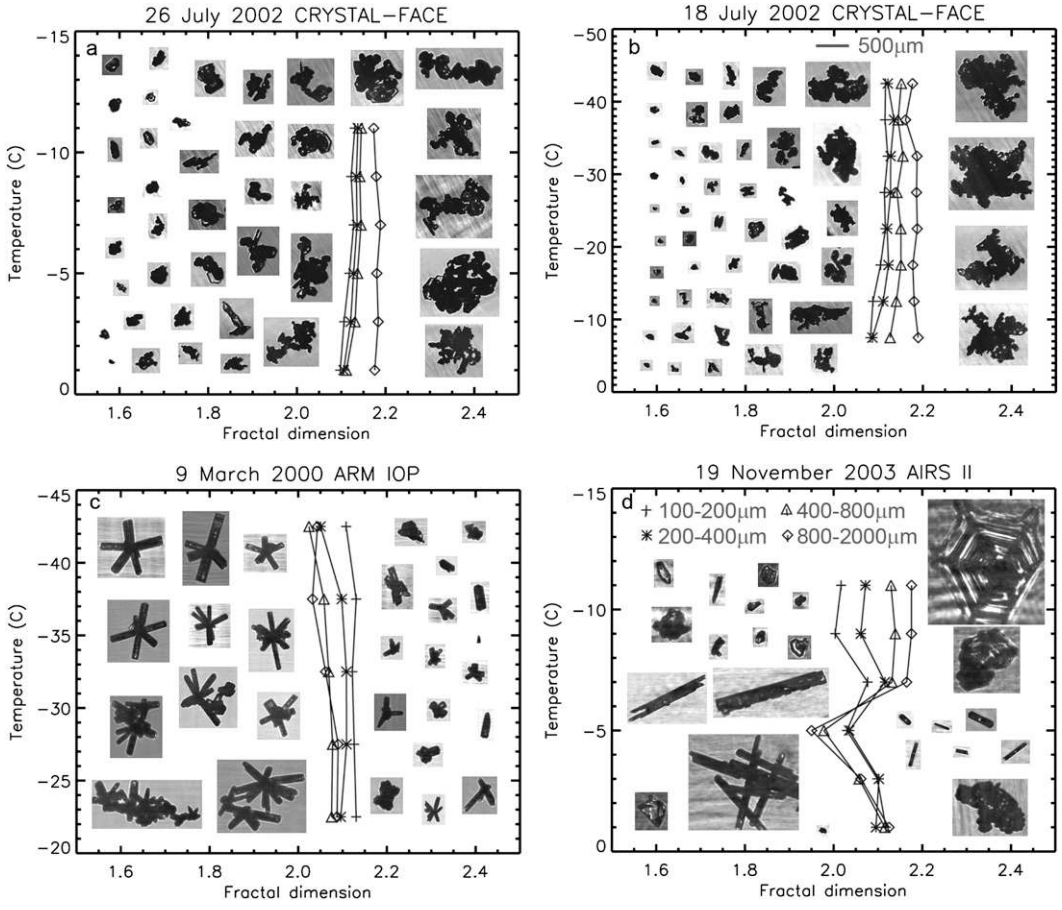

FIG. 7. Ice particle images and fractal dimension calculations for particle images for four research flights. The four lines represent the median fractal dimension values calculated for particles in the four different size ranges in D. The CPI images are displayed at observed temperatures with the particle images sorted by size in the same way that the fractal dimension values lined up at respective temperature levels.

particles had higher fractal dimensions and the largest had lower fractal dimension values. For the AIRS-2 case (AIRS-5, Fig. 4) where large pristine needles, plates, and dendrites were observed, the fractal dimension values changed distinctly in different temperature regimes depending on the particle habits. The needle shaped particles, which were the dominant particle shape at the −5°C level (see Fig. 6d, $T = -5$°C), had distinctly lower fractal dimension values than the plates at −12°C.

c. *Improved mass–dimensional relationships*

Drawing upon the CVI (CSI)-particle probe comparisons and fractal analysis, we take the power in the mass–dimensional relationship to be 2.1. With this assumption, coefficients that provide a better match to the observations than provided by the BF95 coefficients can be found. Partitioning the data for synoptically generated ice clouds into ''cold topped'' (ARM, bullet rosettes, and spatial particles; $T \leq -25$°C) and relatively ''warm topped'' (AIRS, C3VP, columns, planar crystals, and needles; $T > -25$°C), and considering only the convectively generated ice clouds outside of the convective regions (CF, TC4), then

$$m = aD^{2.1}, \tag{8}$$

Where, in cgs units, a is found by finding a value that provides a (median) ratio of measured to calculated IWCs of 1.0: $a = 5.74 \times 10^{-3}$ (cold, where for $D >$ 0.0073 cm, the particle density is below that for spherical ice), $a = 3.59 \times 10^{-3}$ (warm, $D > 0.0043$ cm), and $a = 6.30 \times 10^{-3}$ (convectively generated, $D > 0.0081$ cm). For cases within and in the immediate vicinity of deep convection, $a = 0.0110$ (NAMMA convection, $D >$ 0.0151 cm). With the exception of the tops of the cold layers sampled where the a coefficient might depend on distance below cloud top (Fig. 7c) and localized regions of habit changes may be observed (Fig. 7d), the relationships improve upon the BF95 values (Fig. 8).

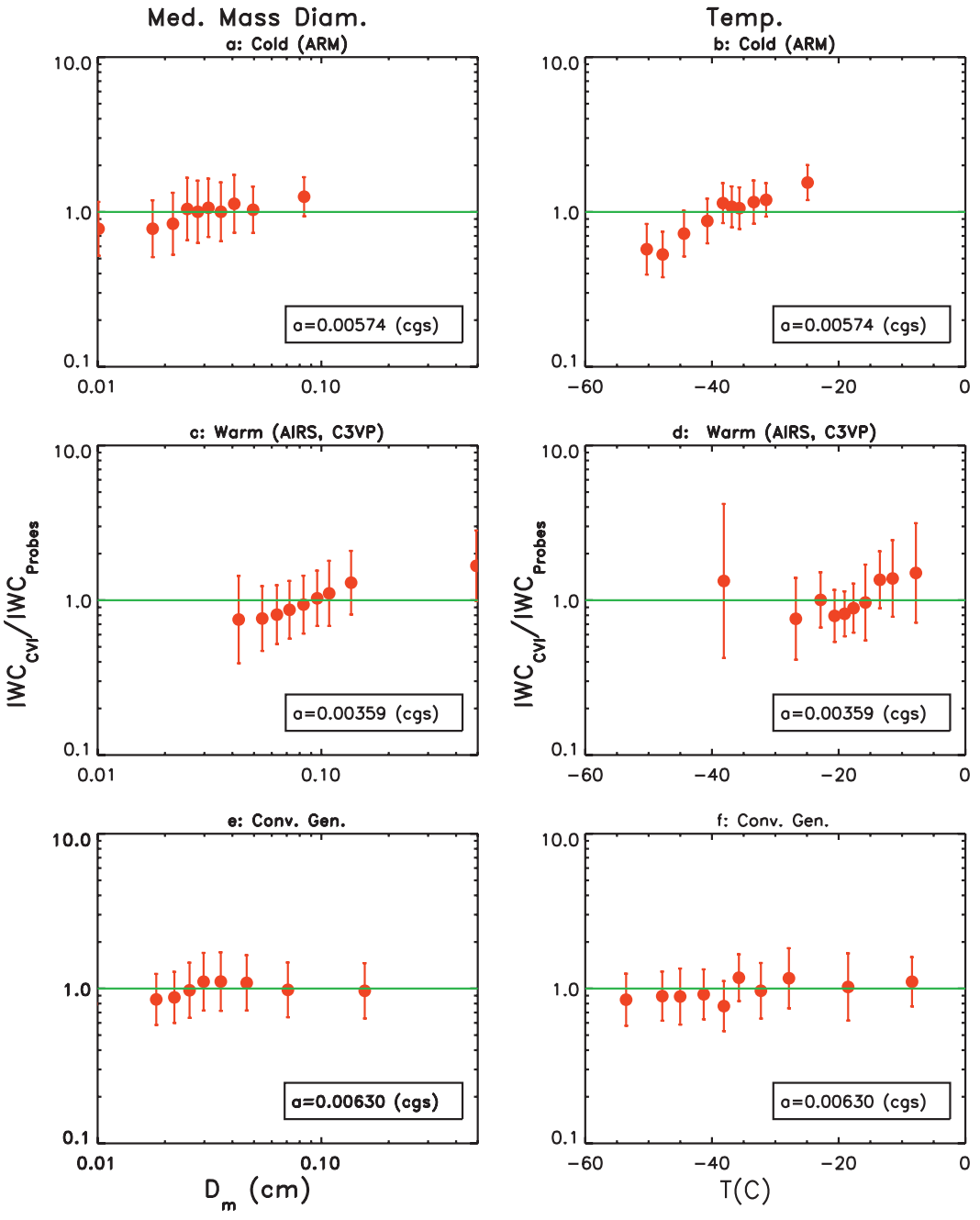

FIG. 8. As in Figs. 6a,d, but using improved estimates of the coefficient a for $b = 2.1$. The results are divided according to cloud type.

Measurements from active remote sensors such as spaceborne radar may not have information available to specify which type of cloud is being viewed;[1] therefore, we have developed relationships that can be applied to all cloud types, with the exception of the regions associated directly with deep convection. We have grouped together the data from all field programs and evaluate the results in terms of the IWC and temperature to look for obvious trends. For the composite dataset, the curve

$$m = 0.005\,28D^{2.1} \tag{9}$$

[1] We suggest that probability distribution functions (PDFs) are developed that represent radar reflectivity as a function of temperature for ice clouds formed by 1) deep convection and 2) large-scale uplift. Such PDFs can presumably be used to identify cloud formation mechanism and appropriate (a, b) pairs.

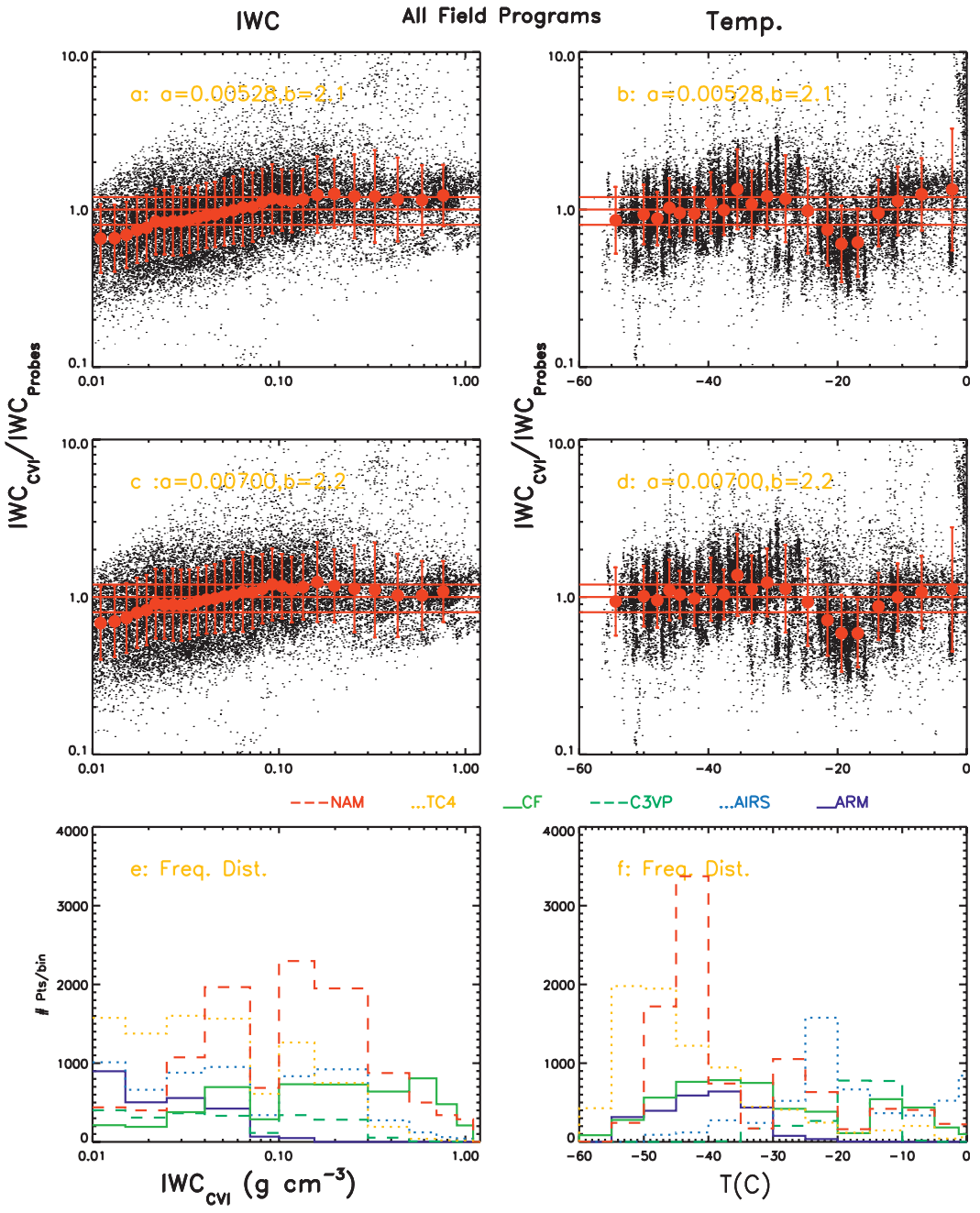

FIG. 9. (a)–(d) As in Fig. 6, but for the composite dataset for all field program, and with IWC as the abscissa in (a) and (c), where (a),(b) $b = 2.1$ and (c),(d) $b = 2.2$, with a coefficients shown. (e),(f) Number of 5-s average PSDs from each field program and shown.

(for $D > 0.0067$ cm) produces results that fit the observations reasonably well across the range of IWCs and temperatures (Figs. 9a,b). Somewhat better results are obtained for the composite dataset with $b = 2.2$ rather than with $b = 2.1$ (Figs. 9c,d versus Figs. 9a,b):

$$m = 0.007\,00D^{2.2} \qquad (10)$$

(for $D > 0.0051$ cm). Deviations from the 1:1 ratio noted in Figs. 9a,d are inevitable and largely related to data acquired from specific sampling flights and field programs (Figs. 9e,f): for example, at low IWC and T, underestimated IWC values [IWC CVI (CSI) > IWC PSD] are largely due to the remnants of convection associated with the TC4 anvils; also, all liquid water regions associated

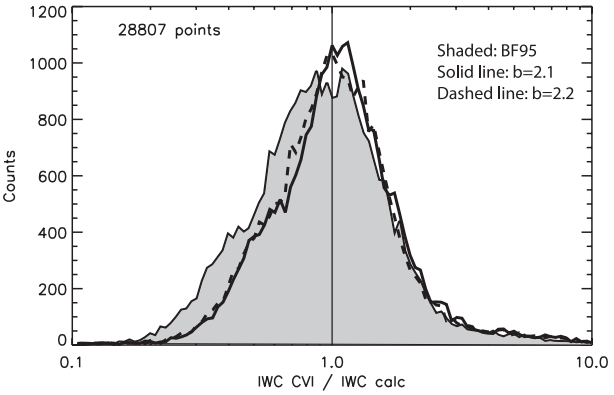

FIG. 10. Frequency distributions of the ratio of IWC (CVI) to IWC derived from the PSDs using the BF95 approach and the $m(D)$ relationship given by Eqs. (9) and (10) for the composite dataset from all field programs.

with the AIRS-2 flights at temperatures from about −15° to −20°C where the liquid water contents are relatively low (~0.02 g m^{-3}) may not have been removed from the dataset and would have been contributed to the CVI (CSI) but not the particle probe IWCs.

Figure 10 compares frequency distributions of the ratio of IWC measured to IWC derived from the BF95 $m(D)$ relationship and those given by Eqs. (9) and (10) for the complete set of 28 800 5-s average data points. The new relationships produce narrower distributions than use of the BF95 relationships with strong peaks near a ratio of unity rather than a broad peak near 0.9. The coefficient 2.2 produces slightly better results than 2.1 but either improves upon the BF95 results.

5. Conclusions

This study has examined how the mass–dimensional relationships of ensembles of ice particles observed in ice cloud layers vary over a broad range of ice cloud conditions. We show that the widely used relationship evaluated by BF95, when applied to measured particle size distributions, reasonably represents the mean ice water content (as measured). Nonetheless, a wide range of (a, b) pairs, with $1.5 < b < 2.5$, can fit the observations. However, the BF95 pairs and most other (a, b) pairs fail to accurately capture dependences of mass on particle size and temperature. These dependences are crucial for accurately deriving other moments of the PSDs, particularly radar reflectivity Z_e and precipitation rate R, and therefore retrievals of IWC or R based on Z_e for which this relationship has been widely used are subject to considerable error.

Ice particles ensembles observed in most ice clouds contain a variety of shapes, are generally not pristine, and are often aggregated and composed of particles with various degrees of riming. As a result, $m(D) = aD^b$ relationships developed for pristine habits generally do not apply. Our observations and fractal analysis suggest that an exponent b of about 2.1, which we find for bullet rosettes and aggregates in general, fit the data for ensembles of particles in both stratiform and convective cloud types over a wide range of temperatures and particle sizes. The coefficient a is about a factor of 2 higher for convectively generated versus stratiform ice clouds as a result of a greater degree of aggregation, complexity of the crystal shapes, and degree of riming. Vertical mixing due to vertical motions produces a uniformity in the $m(D)$ relationship with temperature and size.

Our results are consistent with the growing body of evidence that ice particle masses are higher in convectively generated than stratiform ice clouds (e.g., Bouniol et al. 2010). In the stratiform clouds, localized areas of high concentrations of single particle habits and their aggregates (e.g., needles) can lead to marked deviations when compared to a well-mixed cloud. This result clearly demonstrates that particle habit and particle formation mechanism must be considered when understanding the mass dimensional characteristics of particle ensembles. Average relationships developed from the composite of data from all field programs provide a means of estimating IWCs from particle size distributions when knowledge of the cloud formation mechanism is unavailable.

Acknowledgments. Financial support was provided by the CloudSat Project Office (Deborah Vane), NASA Awards NNX07AQ85G and NNX08AH57G (Hal Maring), and the National Science Foundation Science and Technology Center for Multiscale Modeling of Atmospheric Processes, managed by Colorado State University under cooperative agreement ATM-0425247. Comments and suggestions by Phil Brown are greatly appreciated.

APPENDIX

Identification of Small Ice and Droplet Regions

In this appendix we examine the relationship between the IWC contained in small (<50 μm) and large particles and based on the analysis identify regions where there is appreciable IWC contained in small particles.

Large ice shatters on the inlets of the small particle probes. Heymsfield (2007) and Heymsfield et al. (2009) showed that in ice clouds the following empirical relationships represent the shattering effect:

$$\mathrm{IWC}_s = \mathrm{IWC}_{\mathrm{true}} + c_m \mathrm{IWC}_{\mathrm{2D}}, \qquad \text{(A1)}$$

where IWC_s is the IWC derived by assuming that all particles measured by the small-particle probes are solid

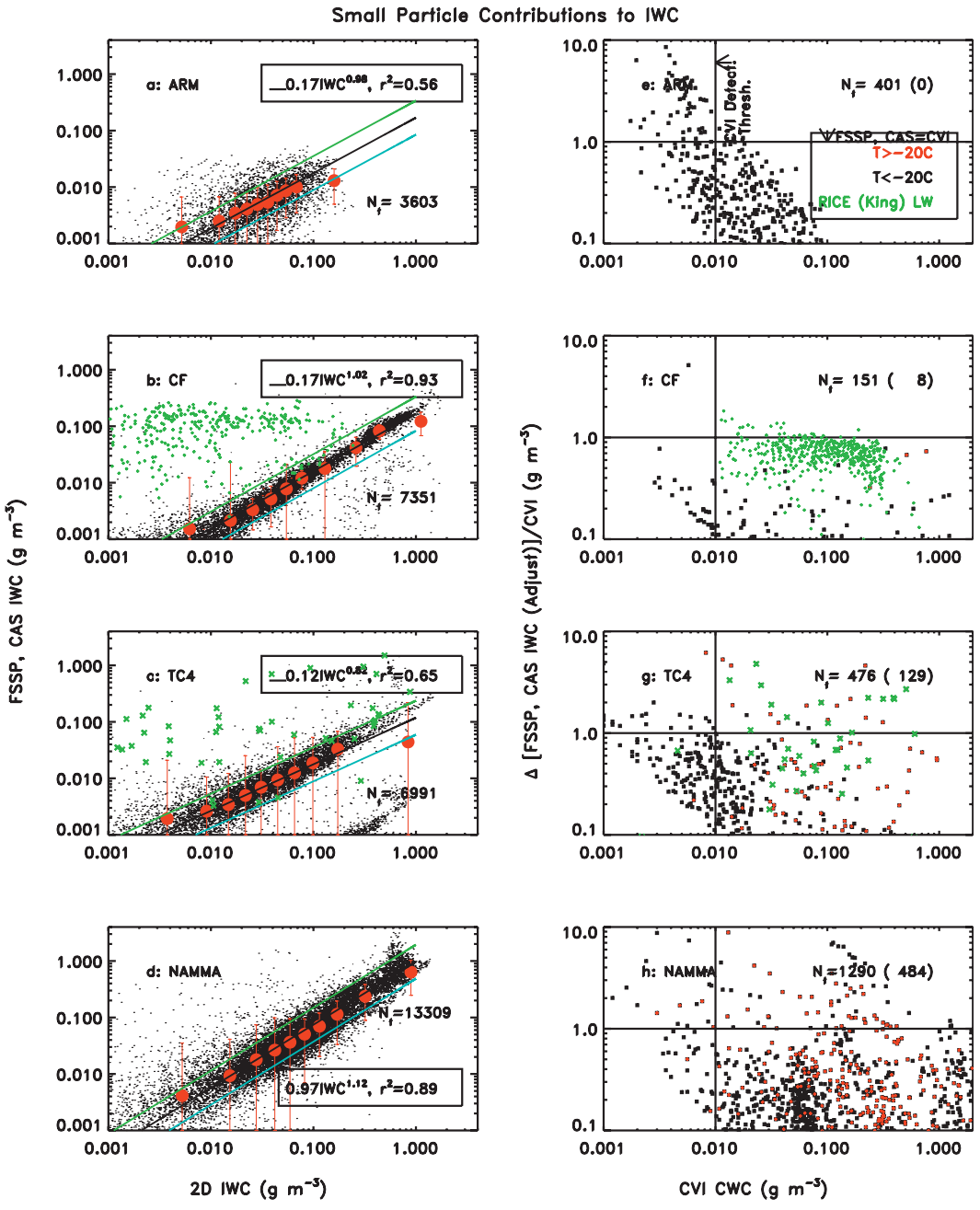

FIG. A1. Estimates of the contributions of small particles to the total IWC. (left) Relationship between the IWC in small and 2D-size particles. Fits to the data and green line denoting the shattering threshold are shown. Total number of points considered for each program and regions of liquid water detection are shown. (right) Ratio of IWC or LWC in small particles (amount above the shattering threshold) divided by the CVI CWC as a function of the IWC. Total number of points in each sample and number of points where temperatures are above −20°C (parentheses) are shown.

ice spheres, IWC_{true} is the actual IWC contained in small particle sizes, c_m is the "shattering coefficient," empirically derived, and IWC_{2D} is the IWC contained in 2D probe sizes; it is not known precisely. If the small particles are true liquid droplets but large ice is present, then LWC_{true} replaces IWC_{true}.

Application of this concept to the particle probe data collected during the ARM, CF, TC4, and NAMMA field campaigns indicates shattering coefficients of 0.17, 0.17, 0.12, and 0.97, respectively (Figs. A1a,c,e,g). For all of these field programs but NAMMA, data on the presence of supercooled liquid water were available. Where

supercooled water is present the associated points fall clearly above the lines representing 1.5 times the shattering coefficient. Other points that fall well above the line representing shattering (e.g., where temperatures are −40°C and below) are likely small ice, the amount of IWC given approximately by their vertical offset above the shattering line.

We use a value of c_m of 1.5 times the amount given by the shattering coefficients to comfortably represent the shattering signature. The right panels of Fig. A1 derive the associated IWCs that lie above the shattering curve as a function of the CWC measured by the CVI (CSI). The ordinate is the amount above the IWC shattering signature normalized by CWC measured by the CVI (CSI). This amount represents the approximate fraction of the total IWC in small particles. Many of these points are in regions detected to be liquid water and so there are clear indications of liquid water, the amounts of which might be underestimated by 10%. Of the total number of intervals with IWCs within the CVI's (CSI's) effective sampling range (left panels), only a small percentage of the points lie above the shattering curve (numbers given in right panels) and relatively few are at temperatures −20°C and above (numbers in parentheses). The largest number of ''warm'' points is from NAMMA and the highest contributions to the IWC in small particles are also from NAMMA. In the analysis given in sections 3 and 4, those points on the right side of Fig. A1 are omitted.

REFERENCES

Bouniol, D., J. Delanoë, C. Duroure, A. Protat, V. Giraud, and G. Penide, 2010: Microphysical characterisation of West African MCS anvils. *Quart. J. Roy. Meteor. Soc.,* **136,** 323–344.

Brown, P. R. A., and P. N. Francis, 1995: Improved measurements of the ice water content in cirrus using a total-water probe. *J. Atmos. Oceanic Technol.,* **12,** 410–414.

Falconer, K., 2003: *Fractal Geometry: Mathematical Foundations and Applications*. Wiley, 337 pp.

Field, P. R., A. J. Heymsfield, and A. Bansemer, 2006: Shattering and particle interarrival times measured by optical array probes in ice clouds. *J. Atmos. Oceanic Technol.,* **23,** 1357–1371.

Heymsfield, A. J., 2007: On measurements of small ice particles in clouds. *Geophys. Res. Lett.,* **34,** L23812, doi:10.1029/2007GL030951.

——, and M. Kajikawa, 1987: An improved approach to calculating terminal velocities of platelike crystals and graupel. *J. Atmos. Sci.,* **44,** 1088–1099.

——, and J. Iaquinta, 2000: Cirrus crystal terminal velocities. *J. Atmos. Sci.,* **58,** 916–938.

——, and C. D. Westbrook, 2010: Advancements in the estimation of ice particle fall speeds using laboratory and field measurements. *J. Atmos. Sci.,* **67,** 2469–2482.

——, A. Bansemer, C. G. Schmitt, C. Twohy, and M. R. Poellet, 2004a: Effective ice particle densities derived from aircraft data. *J. Atmos. Sci.,* **61,** 982–1003.

——, C. G. Schmitt, A. Bansemer, D. Baumgardner, E. M. Weinstock, J. T. Smith, and D. Sayres, 2004b: Effective ice particle densities for cold anvil cirrus. *Geophys. Res. Lett.,* **31,** L02101, doi:10.1029/2003GL018311.

——, A. Bansemer, and C. H. Twohy, 2007: Refinements to ice particle mass dimensional and terminal velocity relationships for ice clouds. Part I: Temperature dependence. *J. Atmos. Sci.,* **64,** 1047–1067.

——, ——, G. Heymsfield, and A. O. Fierro, 2009: Microphysics of maritime tropical convective updrafts at temperatures from −20° to −60°C. *J. Atmos. Sci.,* **66,** 3530–3562.

Hogan, R. J., M. P. Mittermaier, and A. J. Illingworth, 2006: The retrieval of ice water content from radar reflectivity factor and temperature and its use in evaluating a mesoscale model. *J. Appl. Meteor. Climatol.,* **45,** 301–317.

Isaac, G. A., and Coauthors, 2005: First results from the Alliance Icing Research Study II. *Proc. AIAA 43rd Aerospace Sci. Meeting and Exhibit,* Reno, NV, AIAA, 2005-0252. [Available online at http://www.radiometrics.com/isaac_aiaa05.pdf.]

Kajikawa, M., 1982: Observation of the falling motion of early snow flakes. Part I: Relationship between the free-fall pattern and the number of component snow crystals. *J. Meteor. Soc. Japan,* **60,** 797–803.

Lawson, R. P., E. J. Jensen, D. L. Mitchell, B. Baker, Q. Mo, and B. Pilson, 2010: Microphysical and radiative properties of tropical clouds investigated in TC4 and NAMMA. *J. Geophys. Res.,* **115,** D00J08, doi:10.1029/2009JD013017.

Lin, Y.-L., R. D. Farley, and H. D. Orville, 1983: Bulk parameterization of the snow field in a cloud model. *J. Climate Appl. Meteor.,* **22,** 1065–1092.

Locatelli, J. D., and P. V. Hobbs, 1974: Fall speeds and masses of solid precipitation particles. *J. Geophys. Res.,* **79,** 2185–2197.

Mitchell, D. L., 1991: Evolution of snow-size spectra in cyclonic storms. Part II: Deviations from the exponential form. *J. Atmos. Sci.,* **48,** 1885–1899.

——, 1996: Use of mass- and area-dimensional power laws for determining precipitation particle terminal velocities. *J. Atmos. Sci.,* **53,** 1710–1723.

——, R. Zhang, and R. L. Pitter, 1990: Mass-dimensional relationships for ice particles and the influence of riming on snowfall rates. *J. Appl. Meteor.,* **29,** 153–163.

Schmitt, C. G., and A. J. Heymsfield, 2009: The size distribution and mass weighted terminal velocity of low-latitude tropopause cirrus crystal populations. *J. Atmos. Sci.,* **66,** 2013–2028.

——, and ——, 2010: Dimensional characteristics of ice crystal aggregates from fractal geometry. *J. Atmos. Sci.,* **67,** 1605–1616.

Sekhon, R. S., and R. C. Srivastava, 1970: Snow size spectra and radar reflectivity. *J. Atmos. Sci.,* **27,** 299–307.

Takahashi, T., and N. Fukuta, 1988: Supercooled cloud tunnel studies on the growth of snow crystals between −4° and −20°C. *J. Meteor. Soc. Japan,* **66,** 841–855.

——, T. Endoh, G. Wakahama, and N. Fukuta, 1991: Vapor diffusional growth of free-falling snow crystals between −3° and −23°C. *J. Meteor. Soc. Japan,* **69,** 15–30.

Toon, O. B., and Coauthors, 2010: Planning, implementation, and first results of the Tropical Composition, Cloud and Climate Coupling experiment (TC4). *J. Geophys. Res.,* **115,** D00J04, doi:10.1029/2009JD013073.